Aero-propulsive performance improvement of H_2 powered UAS

Nikola Gavrilovic*, Phassawat Leelaburanathanakul, Javier Cuadrado, Jean-Marc Moschetta
ISAE-SUPAERO, University of Toulouse, 31400 Toulouse, France

Abstract

Performance analysis and possible improvements of a long-range unmanned aircraft system powered by fuel cell are investigated using CFD, with the study focusing on the feasibility of crossing the Atlantic Ocean. The motivation behind this aircraft is to demonstrate the capability of the hydrogen fuel cell as an alternative fuel source and to create a case for future commercial and civilian aircraft. The existing hydrogen-powered UAS design is benchmarked and an in-depth analysis of several aerodynamic structures for performance improvement in cruise. The requirements of a 3000 km range, a maximum mass of 25 kg, and hydrogen as a primary energy source, are used as inputs for the conceptual design phase and performance evaluation. The propulsion set, including the propeller geometry and the electric motor, has been optimized for cruise conditions. A detailed study of integrated propeller emplacement has been investigated, showing significant benefits in efficiency.

1 Introduction

The project Drone Mermoz aims to analyze the feasibility of an unmanned aircraft system powered by hydrogen fuel cells that have the capability of crossing the Atlantic Ocean. This route has been selected as it has historical significance; it was used by the French aviation company, Aeropostale in the 1930s and to date has only been crossed by UAS powered with internal combustion engines. The objectives of this project are to design a long-range UAS featuring hydrogen fuel cell-based propulsion, capable of flying from Dakar to Natal (3000 km) and being sufficiently lightweight to be within the certification category allowing beyond the line of visual sight.

Unmanned aircraft systems (UAS) have become instrumental tools for missions in various military, civil and commercial fields. Current generation electrical powered unmanned aircraft systems are limited in terms of range and endurance due to the low energy density of their lithium-based batteries. However, many UAS applications require high range and endurance capabilities for intelligence, surveillance and reconnaissance. This demand for flights which last for considerable periods of time without the need to frequently land coupled with efforts to minimize environmental impact and the benefits of a low thermal and noise signature, make long range electrical aircraft desirable. An emerging source of electrical energy with the potential to solve the limitations of batteries is hydrogen fuel cells. They offer compelling value for unmanned aircraft systems due to the ability to provide approximately five times more power per flight hour for the same weight as lithium based batteries, as well as offering improved reliability and reduced maintenance when compared to small internal combustion engines. Some recent example of hydrogen powered aircraft can be found in [1, 2, 3, 4, 5, 6, 7].

*Email address(es): nikola.gavrilovic@isae-supaero.fr

2 Context

2.1 Performance improvement of a clean aircraft

A preliminary design study of an ultra-long-range drone capable to cross the Atlantic ocean by using fuel cells and hydrogen as a primary energy source has been investigated previously by Gavrilovic et. al. [8] and is shown in Figure 1.

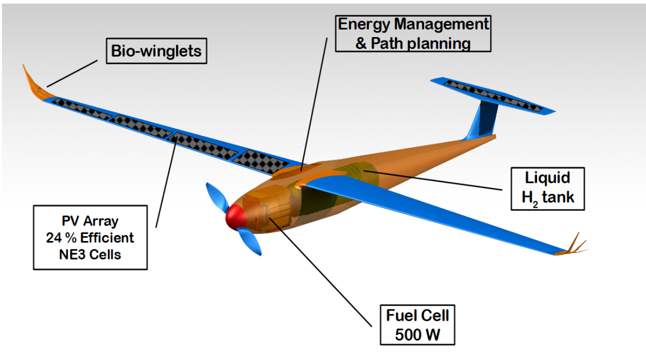

Figure 1: Drone Mermoz v1 - 12 kg and 3.6 m span demonstrator of technology.

Further development of a design procedure led to a combination of analytic approach and optimization cycle. The structural mass estimation was performed using the Gundlach [1] equations, with the iteration of the propulsive system in the function of available energy required for the journey. Once the estimated mass was determined, a parametric study was conducted to find adequate ranges of aircraft size which have been used in the optimization cycle. The last part of the preliminary design procedure was an optimization cycle working with a modified version of AVL which takes into account viscous effects integrated into an OpenMDAO genetic algorithm environment.

A final result of the optimization cycle was a 12 kg aircraft with wing-span of 3.6 m, having maximum lift-to-drag ratio of around 25. The clean aircraft named Drone Mermoz v1 and shown in Figure 2 is designed for following mission requirements:

- Must be able to cross the distance of 3000 km with liquid hydrogen as a primary energy source.
- To have a total mass of less than 25 kg.
- Must use hydrogen fuel cell as primary energy source

The performance improvement of this given clean aircraft is related to design, development and integration of certain aerodynamic structures. The main objective is to improve the aircraft endurance and range. Therefore, the CFD analysis of this clean aircraft will be performed in order to be compared with improved design such as:

- Fuselage-wing junction optimization (design of "Karmans")
- Implementation of winglets (comparison between bioinspired wing-tip feathers and blended winglet).

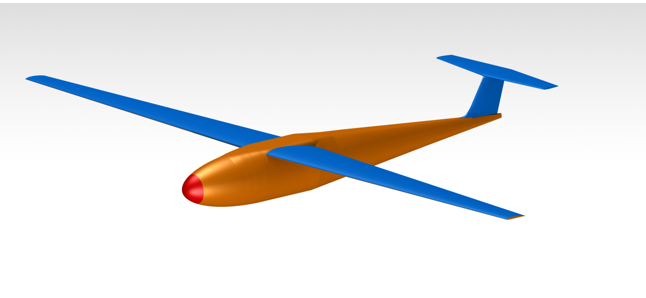

Figure 2: Drone Mermoz v1 - clean aircraft.

The main geometrical, aerodynamic and propulsive parameters of Drone Mermoz v1 are presented in table 1.

2.2 *Propulsive optimization*

The main objectives of the propulsive optimization study are a choice of the propeller, motor, and a more interesting part of fuselage integration that will be presented here. This study aims to investigate the the effect of fuselage body on the performance of the propeller according to different emplacements. A potential benefit in increased propulsive efficiency and thrust can come from two different points. The first is related to a covering of around 25 % of propeller root as this part mainly generates drag, while the second is related to the investigation of flow deviation to overall propeller performance. Therefore, the study will focus on propeller integration in already existing fuselage design (without fuselage shape modification), thus avoiding standardized spinners.

Parameter	Value	Unit
V_c	23	$[m/s]$
Wingspan	3.6	$[m]$
Fuselage length	1.7	$[m]$
Wing surface	0.65	$[m^2]$
AR	20	—
Total mass	12	$[kg]$
Structural mass	4.5	$[kg]$
$C_{Lcruise}$	0.57	—
$C_L/C_{D_{max}}$	25	—
ρ	1.2	$[kg/m^3]$
Fuel cell	HES AEROSTAK 500	—
LH_2 reservoir	7	$[l]$
Range	3200	$[km]$

Table 1: Drone Mermoz V1.

3 GEOMETRY AND MESH PREPARATION

3.1 *Boundary conditions and domain*

The dimensions of the domain are chosen to be sufficiently large to allow enough space around the geometry of interest so that the perturbations in the flow field do not interfere with the boundaries. The domain shown in Figure 3 was selected so that the domain should allow a minimum of 2 times the geometry's length in the upstream direction, 5 times in the downstream direction, and 2 times in width.

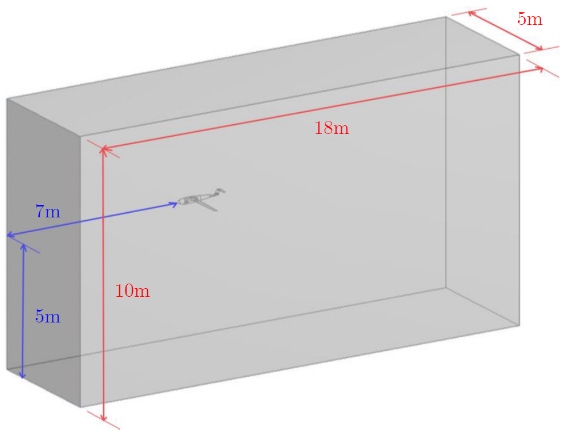

Figure 3: Flow domain.

After the definition of the physics continua to be used for the computation, the boundary conditions of the mesh domain are specified. Using the surface parts that were named during the mesh construction process in the ICEM-CFD software, the definition of types, physics conditions, and values of the boundary condition is straightforwardly inputted into the solver software. A diagram describing the different boundary conditions used for simulations with a positive angle of attacks is shown in Figure 4 below.

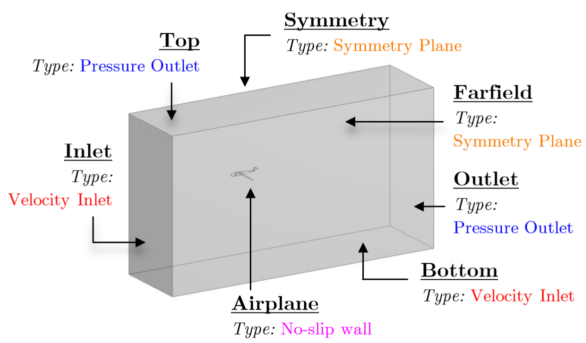

Figure 4: Boundary conditions.

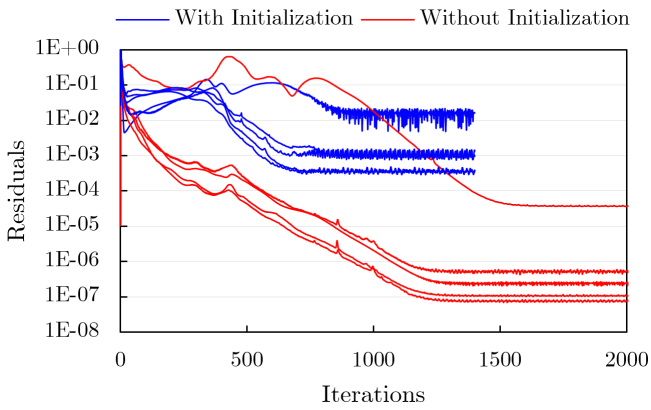

Figure 5: Residuals.

3.2 *Computational setup*

For the simulations without an angle of attack, the Top, Bottom, Symmetry, and Farfield boundary condition type is set to a symmetry plane. In STAR-CCM+, the tangential shear stress at a symmetry boundary is fixed to zero. The velocity face value at the boundary is extrapolated from the parallel component of the flow of the adjacent cells using reconstruction gradients. This ensures that there will be no flow passing through a symmetry boundary. The methodology of the pressure outlet boundary condition is similar as it also extrapolates the velocity of the interior cells to the boundary face using reconstruction gradients. Since the reference pressure of the simulation is already fixed at 101,325 Pa, the Outlet pressure specification is set to 0 Pa gauge.

The criterion that used to ensure the solution's convergence is the residuals shown in Figure 5 of the transport equations. In CFD analysis, residuals quantify the local imbalances of variables at each control volume. The velocity inlet flow direction was specified using normalized x and y components. For the simulations with a negative angle of attack on the airplane, the Bottom boundary condition is switched to a pressure outlet and the Top boundary condition is set to a velocity inlet. For an airplane model, the angle of attack range is from $-4°$ to $+12°$, giving a total of 12 simulations. Moreover, an extra simulation will be conducted at the drone's operating point.

3.3 *Mesh study*

This chapter will provide an extra effort in finding out the balance between the solution accuracy and the computational time. It must also be pointed out that the time required to mesh geometry is not insignificant either. For the mesh size used in this project shown in Figure 6, a full mesh generation time on a personal computer takes approximately 1.5 to 2 hours, including the volume and prism generation. This value can extend up to 2.5 hours when generating the finer mesh for the convergence study. The geometry used for this project's mesh independence study is the aircraft shown in Figure 2. The mesh is varied by re-sizing the parts mesh setup, as well as the volumetric refinement on all density regions. There is a total of 5 mesh variations, gradually increasing from 8.5 million cells to 15.9 million cells. Since the prism layers are

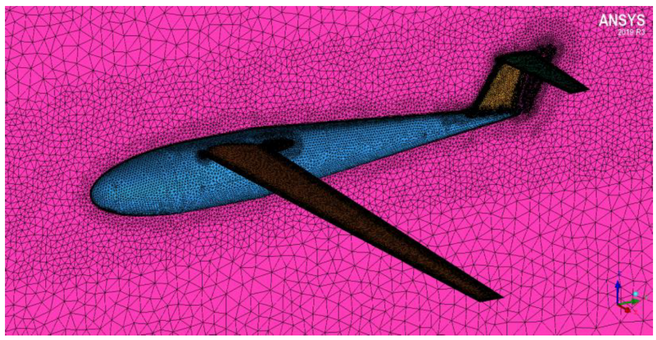

Figure 6: Surface mesh on the first baseline (v1) version of the airplane.

sized according to the flat-plate boundary layer theory, it is crucial that the wall y+ is verified after the simulation is computed to see if further refinements are necessary. To ensure that there is at least one cell to resolve the flow within the viscous sub-layer of the boundary layer, the wall y+ should not exceed 5. Figure 7 shows the distribution of the wall y+ of all cells adjacent to the airplane's surface. It can be observed that a very large quantity of the cells on the airplane's surface has a y+ value of around 1. As a matter of fact, 77.0 % of all adjacent cells has a y+ value less than 1.2 and 99.0 % has a y+ value less than 1.6. There are only 2 from the total 198,827 adjacent cells that has a y+ value greater than 5 which can be safely considered negligible.

Additionally, a closer inspection of the wall y+ value of the cells on the fuselage at the symmetry plane in Figure 8 shows that most of the cells are less than or equal to 1. The dimensionless velocity profile of the flow above the fuselage at X-position equal to 0.637 meters shown as a magenta line in Figure 8 is examined.

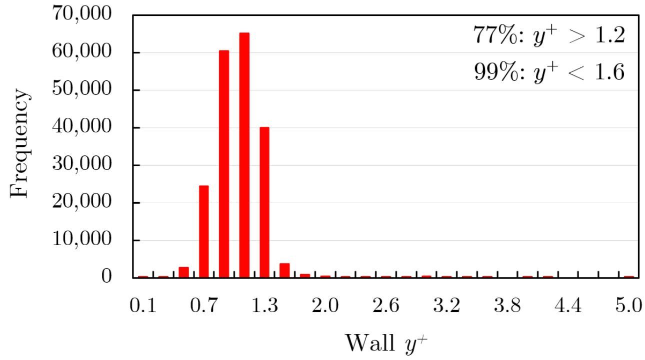

Figure 7: The wall y+ distribution of airplane-adjacent cells.

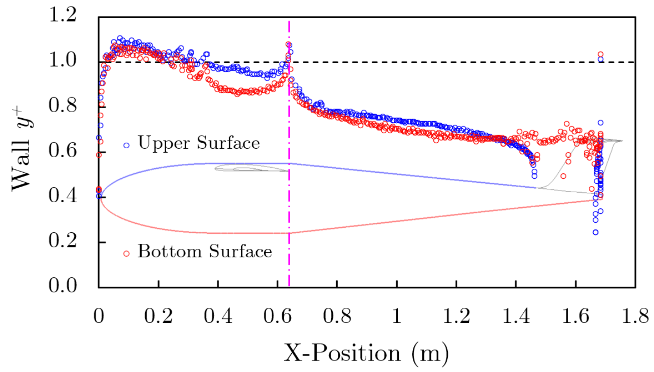

Figure 8: The wall y+ value of the fuselage top and bottom surface at the symmetry plane.

4 RESULTS

4.1 *General performance*

An initial study has been performed to analyze and compare the general performance of the aircraft using both vortex lattice program AVL and previously explained CFD setup. The lift slope curve shown in Figure 9 shows a slight difference in zero angle of attack lift coefficient while having the same lift slope.

The main difference between two methods is shown in Figures 10 and 11 and is coming from difference in drag prediction. A vortex lattice program used in this work is a modified version of AVL, which includes the prediction of viscous drag, where the viscous drag coefficient $c_{vd} = c_{vd}(Re, \alpha_t)$ depended on a chord-based Reynolds number and the total angle of attack α_t. The fact that the total drag prediction of modified AVL depends on the airfoil viscous database previously built, and a choice of default profile drag coefficient added to geometry brings a certain doubt in total coefficient values. On the other hand, with a calculation time of less than a second, the potential for comparative studies and ease of integration in the optimization loop keep modified AVL as a highly desirable tool, especially in the preliminary design phase.

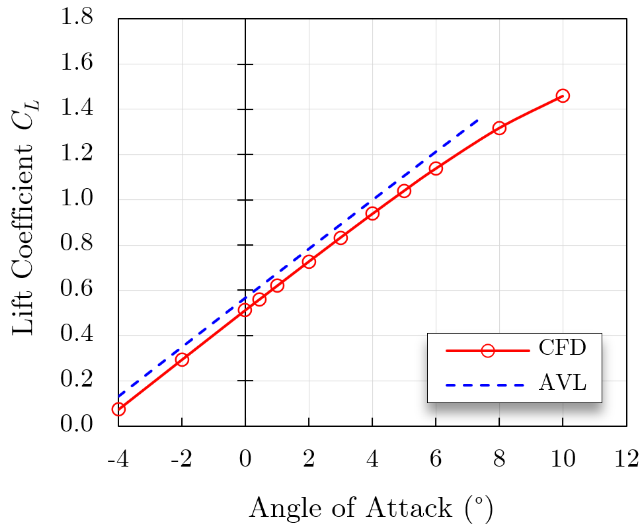

Figure 9: Lift curve.

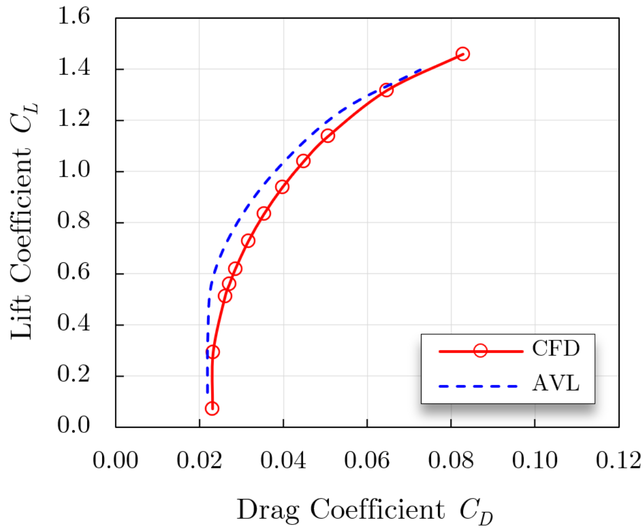

Figure 10: Polar.

The Figure 12 shows a span-wise lift distribution for a trapezoidal wing shown in 2 which is almost elliptical for a chosen tapper ration of 0.36.

Further analysis of fuselage pressure coefficient distribution shown in Figure 13 revealed a small contribution in a lift in the area ahead of the wing. The plot also reveals a peak of a pressure coefficient at the place after wing-fuselage junction where the transition to a rear part of the fuselage-cone is beginning. The conclusion is that this kind of sharp geometrical transition should be avoided in the definitive version which will be fabricated.

Moreover, a total drag decomposition shown in Figure 14

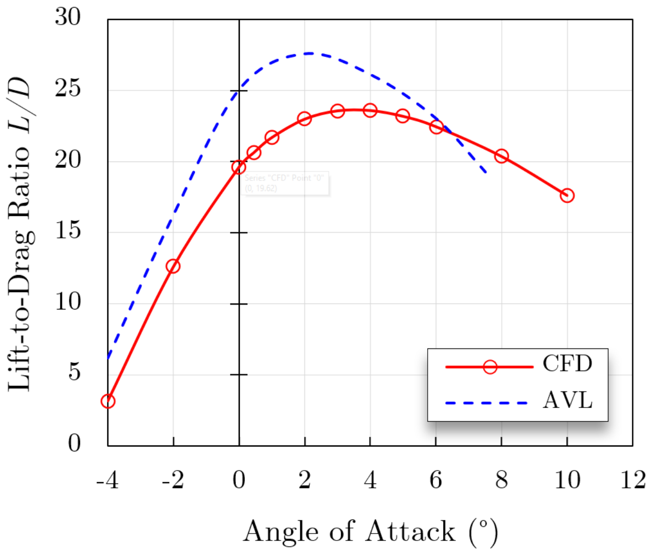

Figure 11: Lift-to-drag ratio.

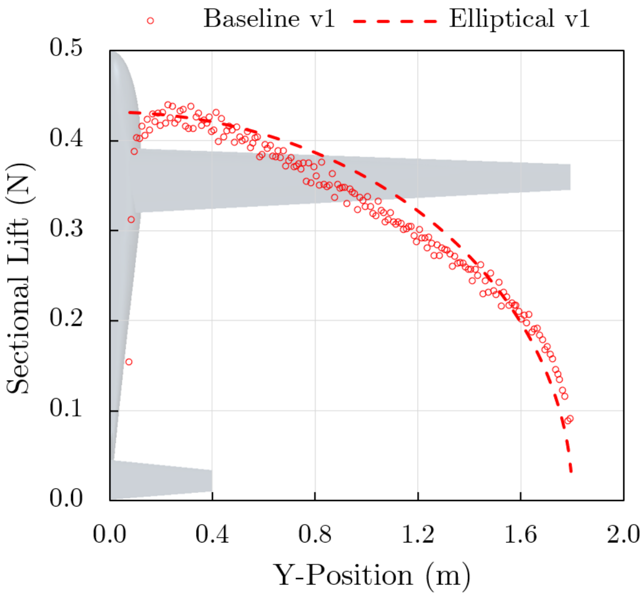

Figure 12: Span-wise lift distribution.

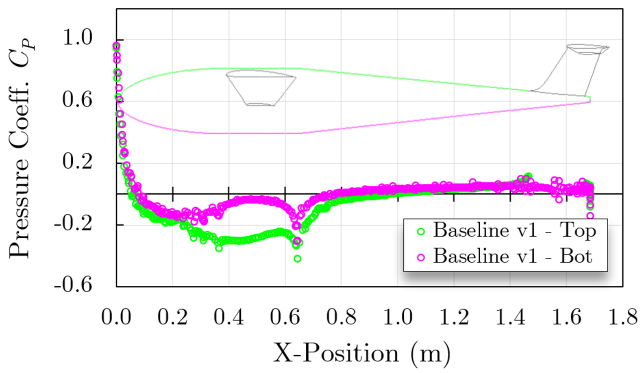

Figure 13: Fuselage pressure distribution.

shows that a 60 % of a total drag is coming from a viscous part, while the other 40 % belongs to a pressure drag. Further analysis of viscous drag decomposition shown in Figure 15 revealed that the majority of viscous drag is coming from a wing due to the biggest part of its wetted surface when compared to other parts of the aircraft.

Finally, a pitching moment coefficient has been shown in Figure 16 for various reference locations. The objective of this study was to determine where is the position of the neutral point and to compare it with prediction coming from AVL. As it can be seen, a point for which the pitching moment coefficient does not vary with angle of attack is located at $x = 0.510m$ from an aircraft nose. This value is less than a 3 % difference than the one coming from an AVL, which moreover confirms the benefits of using AVL in the preliminary design phase.

4.2 Improvement using winglets and karmans

This chapter has been devoted to the exploration of potential aerodynamic structures that could enhance the overall performance of the aircraft, therefore, endurance and range. The previous study shown by Gavrilovic [9] has quantified considerable improvements that can be achieved using winglets on commercial aircraft. However, due to a huge discrepancy in flight conditions, a new study has been conducted adapted to flight conditions of a small drone. It should be noted here that even a benefit of a couple of percent is highly valuable as the aircraft is supposed to fulfill the mission requirement of having more than 3000 km of range. Two different winglet designs have been studied and compared to clean aircraft performance. The first one is a bio-inspired winglet shown in Figure 17 that resembles the eagle wing tip feathers. The second design is a classical blended winglet shown in Figure 18, found on various aircraft types, from small UAVs for lateral stability purposes up to big commercial aircraft for induced drag reduction. Moreover, a smooth karman design have been presented in Figure 19. On top and below the wing it consists of small rounded edge to reduce the surface and such friction drag. At the leading and trailing edge it consists of much larger taper and smooths out the pressure differences: High pressure at the leading and trailing edge, low pressure on top of the wing and around the fuselage. The main objective of the karman is to suppress potential formation of vortex in the rear part of the fuselage-wing junction, and therefore, prevent possible drag sources.

The final comparison between different structures and clean aircraft for cruise operating conditions is presented in Figure 20. It can be seen that the karman design provided around 1 % reduction in total drag. On the other side, winglet structures provide more significant benefits with up to 5 % in

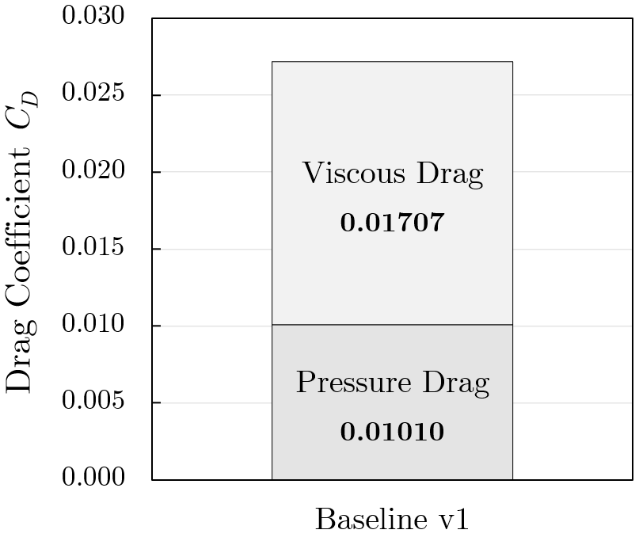

Figure 14: Total drag of the aircraft in cruise.

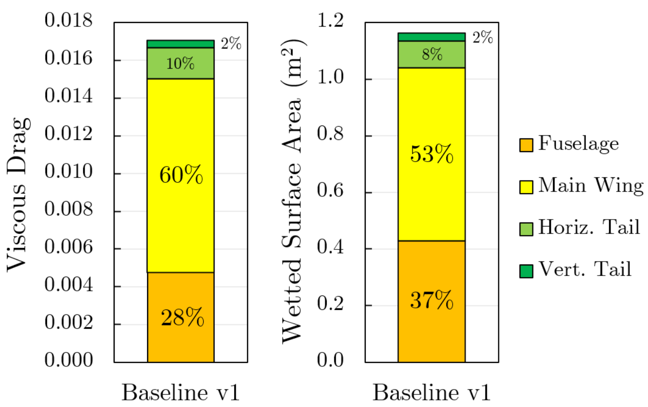

Figure 15: Viscous drag of the aircraft in cruise.

total drag reduction. Moreover, the addition of winglets usually brings around 4-6 % higher lift coefficient for the same angle of attack. That means that the drag can be even more reduced by decreasing the required angle of attack in cruise for a configuration with winglets. Finally, it should be pointed out that a 5 % drag reduction represents a significant achievement, being 150 km out total required 3000 it can be considered as a fuel reserve.

4.3 *Propulsive optimization*

Early design stages focused on finding the optimal propulsive system (propeller + motor combination) for the desired task. Indeed, given the very long-range to achieve, even the slightest improvements of performances can dramatically affect the final output of the mission. To this end, all the propellers listed on the *APC Propeller* website were tested, alone and in combination with the electric *T-Motors* and *Aximotors*, to find the best possible propulsive system.

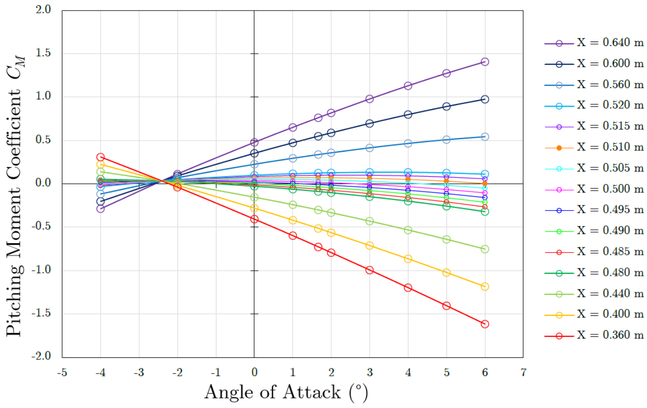

Figure 16: Pitching Moment Coefficient CM vs. angle of attack measured at various points along fuselage axis.

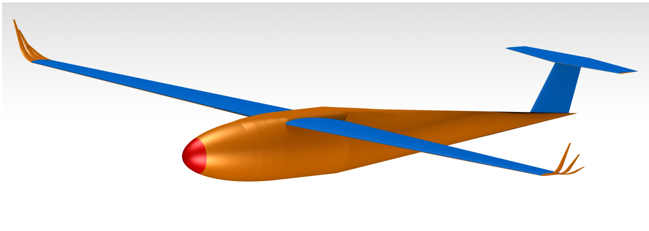

Figure 17: Bio-winglet.

Optimal propellers were found to be around the 20-inch diameter range when rotating at around 3000 rpm. Smaller blades require greater rotational speeds for similar performances, while greater ones can lead to mass increments detrimental to the desired range. While our interest remains still to design an optimal propeller for the desired task, this analysis allows us to identify a promising range of propeller dimensions to analyze, thus making the final design process easier.

Finally, we found that the availability of commercial electric motors is sufficient to find a propeller/motor combination with sufficient performances for the desired task. Furthermore, in case of need, the construction of a dedicated motor is feasible, so we decided to proceed with the design of the optimal propeller, as well as an analysis of the influence of its position in the fuselage in its aerodynamic performances.

We now proceed to study the aerodynamic performance

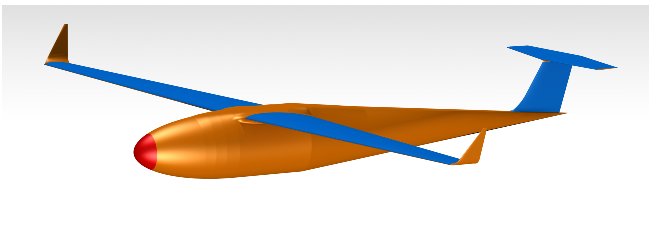

Figure 18: Blended-winglet.

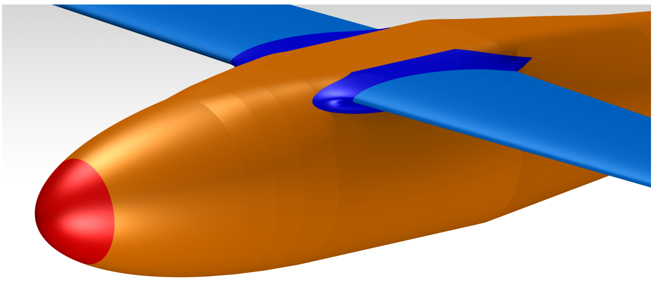

Figure 19: Wing-fuselage junction.

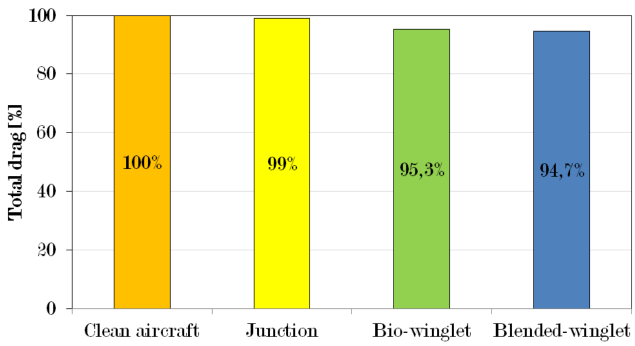

Figure 20: Total drag for different aircraft configurations.

of the optimum propeller, obtained for Drone Mermoz v1, when embedded 50 mm away from the tip of the fuselage. Having verified the viability of using XRotor with a cho-

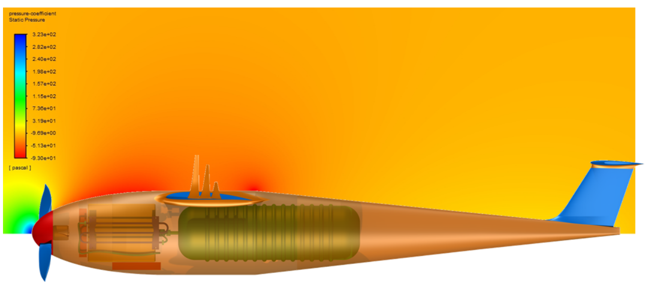

Figure 21: Fuselage pressure distribution.

sen propeller, we proceed to analyze the aerodynamic performance of chosen propeller when embedded in a spinner 50 mm away from the aircraft's nose. XRotor can compute the behavior of a propeller when under a non-uniform stream by being given the flight speed and the additional speed for each radial station. To obtain this speed distribution at the station x=50 mm, an Ansys-Fluent software package has been used. After analyzing the propeller for the non-uniform stream, we obtain the following outcome:

Having seen the beneficial effects of embedding the propeller in a spinner, we seek now to determine the optimal

Parameter	Isolated	Embedded	increment %
Thrust [N]	4.67	4.85	+3.85 %
η_p **[%]**	87.49	91.62	+4.13 %

Table 2: Performance variation of a chosen propeller.

position to place the propeller to fully optimize the performance. To this end, an Ansys-Fluent analysis have been carried out. When moving the propeller backwards, we see that the propeller performances fast degrade. Only in the rearrest part of the ellipsoidal section of the fuselage do we see a slight upgrade of performances when compared with the immediate preceding ones, even if these performances are still worse than those obtained for a propeller embedded 50mm away from the nose, or even an isolated propeller under a uniform stream. The opposite situation is seen when moving the propeller towards the nose, since we obtain an upgrade on the performances. However, there has to be an optimum for these performances, after which they will decay to the values obtained for the uniform stream performances. The evolution of the performances can be seen in Figure 22 and 22.

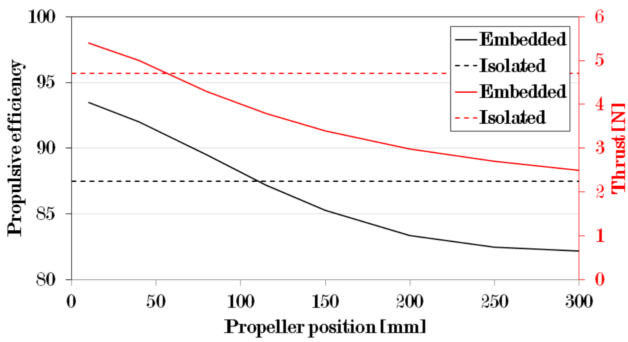

Figure 22: Propeller efficiency and thrust variation with position.

Some conclusions can be extracted from these results:

- While moving the propeller close to the nose yields higher thrusts and efficiency, the increase of thrust also means an increase in the necessary power to fly at the desired speed and omega.
- The most interesting region to place the propeller is the interval $46 < x < 60$ mm, since in this region, the thrust obtained is higher than the one provided by the isolated propeller, while the necessary power to produce this thrust is lower.

Figure 23 show that the propulsive efficiency decreases as we embed a higher section of the propeller into the spinner. This tendency is actually counter-intuitive, since suppressing the inner sections of the blade (which mainly generate drag) should actually lead to increased propulsive efficiency. We, therefore, conclude that the performance variations over the isolated solution are due to the non-uniform velocity profile rather than to suppressing the blade's inner part.

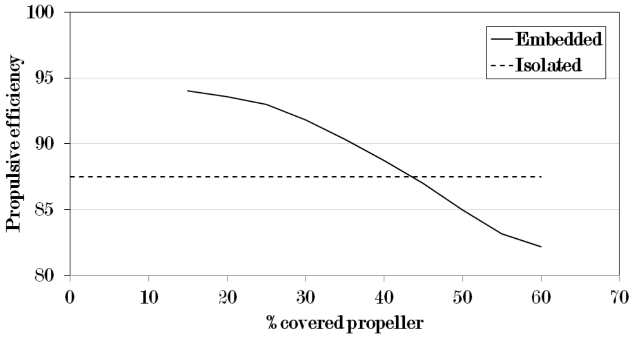

Figure 23: Propulsive efficiency vs. percentage of covered blade for the embedded propeller.

5 CONCLUSION

A performance study of an ultra-long-range drone powered by a fuel cell and hydrogen has been performed using both CFD and vortex lattice methods. The main findings of this study are that significant achievements in drag reduction can be achieved using both blended and bio-inspired winglets. A drag reduction of around 5 % represents a significant gain in overall performance as it can be taken as a fuel reserve in the mission. On the other hand, fuselage-wing junction design brought benefit in a drag reduction of only 1 % which is still significant and to be confirmed in the wind tunnel campaign. A reasonable match was found in neutral point estimation between the two methods with the conclusion that AVL can be further used for such estimations with confidence. Moreover, a study of integrated propeller design showed that the elliptical fuselage tip can contribute to around 4 % gain in propulsive efficiency of a propeller. The benefit of the increased efficiency and thrust of the propeller was found to be due to coverage of around 25 % of the propeller root and deviated flow due to fuselage presence. The next phase of performance investigation will be a wind tunnel campaign of full-scale aircraft, with objective to confirm and verify gains due to application of new aerodynamic structures and propulsion integration.

REFERENCES

[1] J. Gundlach. *Designing Unmanned Aircraft Systems: A Comprehensive Approach*. American Institute of Aeronautics and Astronautics, Reston, VA, 2014.

[2] P. Osenar, J. Sisco, and C. Reid. Advanced propulsion for small unmanned aerial vehicles. Technical report, Ballard Canada, 2017.

[3] Sparkle Tech. Eagle plus vtol 3.5m, 2019. http://www.sparkletech.hk/electric-power/eagle-plus-vtol/.

[4] K. Swider-Lyons, K. MacKrell, J. A. Rodgers, G. S. Page, M. Schuette, and R. O. Stroman. Hydrogen fuel cell propulsion for long endurance small uavs. In *AIAA Centennial of Naval Aviation Forum.*, 2011.

[5] H3 Dynamics. Hywings, 2016. http://www.h3dynamics.com/products/hywings/.

[6] Insitu. Scan eagle capabilities, 2018. https://www.insitu.com.

[7] M. Gatti. Complete preliminary design methodology for electric multirotor. *Journal of Aerospace Engineering*, 30(5):1–15, 2017.

[8] N. Gavrilovic, D. Vincekovic, and J-M. Moschetta. A long range fuel cell/soaring uav system for crossing the atlantic ocean. In *IMAV 2019*, 2019.

[9] N. Gavrilovic, B. Rasuo, G. Dulikravich, and V. Parezanovic. Commercial aircraft performance improvement using winglets. *FME Transactions*, 43(1):1–8, 2015.